Delft University of Technology

Fluidic Force Microscopy and Atomic Force Microscopy Unveil New Insights into the Interactions of Preosteoblasts with 3D-Printed Submicron Patterns

Angeloni, Livia; Popa, Bogdan; Nouri-Goushki, Mahdiyeh; Minneboo, Michelle; Zadpoor, Amir A.; Ghatkesar, Murali K.; Fratila-Apachitei, Lidy E.

Important note
To cite this publication, please use the final published version (if applicable).
Please check the document version above.

Fluidic Force Microscopy and Atomic Force Microscopy Unveil New Insights into the Interactions of Preosteoblasts with 3D-Printed Submicron Patterns

Livia Angeloni, Bogdan Popa, Mahdiyeh Nouri-Goushki, Michelle Minneboo, Amir A. Zadpoor, Murali K. Ghatkesar,* and Lidy E. Fratila-Apachitei**

Physical patterns represent potential surface cues for promoting osteogenic differentiation of stem cells and improving osseointegration of orthopedic implants. Understanding the early cell–surface interactions and their effects on late cellular functions is essential for a rational design of such topographies, yet still elusive. In this work, fluidic force microscopy (FluidFM) and atomic force microscopy (AFM) combined with optical and electron microscopy are used to quantitatively investigate the interaction of preosteoblasts with 3D-printed patterns after 4 and 24 h of culture. The patterns consist of pillars with the same diameter (200 nm) and interspace (700 nm) but distinct heights (500 and 1000 nm) and osteogenic properties. FluidFM reveals a higher cell adhesion strength after 24 h of culture on the taller pillars (32 ± 7 kPa versus 21.5 ± 12.5 kPa). This is associated with attachment of cells partly on the sidewalls of these pillars, thus requiring larger normal forces for detachment. Furthermore, the higher resistance to shear forces observed for these cells indicates an enhanced anchorage and can be related to the persistence and stability of lamellipodia. The study explains the differential cell adhesion behavior induced by different pillar heights, enabling advancements in the rational design of osteogenic patterns.

1. Introduction

Biomaterials topography at micro- and nano-scale is emerging as a potent modulator of cellular responses, including adhesion

L. Angeloni, M. K. Ghatkesar
Department of Precision and Microsystems Engineering
Faculty of Mechanical, Maritime, and Materials Engineering
Delft University of Technology
Mekelweg 2, Delft 2628CD, The Netherlands
E-mail: l.angeloni@tue.nl; m.k.ghatkesar@tudelft.nl
L. Angeloni, B. Popa, M. Nouri-Goushki, M. Minneboo, A. A. Zadpoor, L. E. Fratila-Apachitei
Department of Biomechanical Engineering
Faculty of Mechanical, Maritime, and Materials Engineering
Delft University of Technology
Mekelweg 2, Delft 2628CD, The Netherlands
E-mail: e.l.fratila-apachitei@tudelft.nl

and growth,[1–6] immunoregulation[7,8] and differentiation.[6,9–14] This approach is of great clinical relevance for orthopedic implants where osteoinductive[15–17] and antibacterial[15–16,18] surfaces are required to prevent aseptic and septic failures, thereby ensuring the long-term stability of the implants. Different physical surface patterns at micro- and nano-scale, with specific geometries and spatial distribution, have shown potential for promoting osteogenic differentiation of mesenchymal stromal cells (MSCs) and preosteoblasts in vitro.[9–13]

However, the relationships between patterns characteristics and cell response are not univocal. Subtle variations of the surface roughness and/or the geometrical characteristics of the topographical features can result in substantially different cell responses.[13,17,19–20] In addition, contradictory effects on the osteogenic differentiation of MSCs and osteoprogenitor cells have been reported for different relevant topographies' scales (i.e., cell scale and smaller), suggesting that different feature sizes can act via different cellular mechanisms. Indeed, the osteopontin (OPN) expression after 21 days of incubation was observed to decrease with the increase of the height of the pillars in the nanometer range (i.e., pillar height < 100 nm).[21,22] On the contrary, it has increased with the increase in the pillar height and the decrease of the interspace between pillars in the submicron (i.e., pillar height < 1000 nm) and micron (i.e., pillar height larger than 1.6 µm) range.[14,23]

Substrate physical features can modify the way cellular receptors (integrins) attach to the surface and activate direct or indirect mechanotransduction pathways. These mechanisms involve focal adhesions (FAs) formation, cytoskeleton reorganization, generation of endogenous (intracellular) forces and nuclear translocation of transcription factors, that influence the late cellular functions.[22,24–27] Understanding of the topography-induced mechanotransduction is required for establishing a rational design for osteogenic surfaces. Nevertheless, the lack of systematic studies and the limited quantitative methods available until recently to investigate the biophysics involved in these early interactions, hindered the advances in this area.

Atomic force microscopy (AFM), due to its capability to detect ultralow forces and to be used in a liquid environment,

**ADVANCED
SCIENCE NEWS**

www.advancedsciencenews.com

NANO · MICRO

small

www.small-journal.com

is emerging as a powerful tool for the quantification of the physical properties of living cells.[28–34] However, so far, the AFM techniques were rarely used to investigate the biophysics of living cells interacting with cell instructive topographies. Yang et al. measured the elastic modulus of MSCs cultured on osteogenic and non-osteogenic gratings at different phases of the differentiation process.[35] They found that MSCs cultured on the most osteogenic topographies had the highest elastic modulus before differentiation and the most rapid cell stiffness reduction during differentiation.

In our recent work,[14] we have used single-cell force spectroscopy (SCFS) to quantify for the first time the adhesion force of mouse preosteoblasts (MC3T3-E1) on 3D printed submicron patterns during the first minute of cell attachment. For some of the patterns investigated, we have found a positive correlation between the cell adhesion force and the late ECM mineralization, which suggested a link between the early adhesion mechanisms and the late differentiation behavior. However, due to the intrinsic limitations of the single-cell force spectroscopy (SCFS) technique, we could only quantify the adhesion forces during the first minute of cell–substrate interactions when mostly physical (i.e., electrostatic and hydrophobic) interactions are involved in cell adhesion.[36,37] Nevertheless, the later phase of cell adhesion to the substrates (between a few hours and a few days) plays the most significant role in the activation of the mechanotransduction pathways, involving cell spreading, integrins clustering, FAs formation and cytoskeleton reorganization.[36,37]

Therefore, in this follow-up study, we have performed a more in-depth investigation of the adhesion behavior of MC3T3-E1 cells when cultured on two selected patterns, one that showed osteogenic potential (P1000) and another one with no such properties (P500).[14] The only difference between these patterns is the pillar height: the P1000 pattern has pillars of 1000 nm height whereas the P500 pattern has pillars of 500 nm height. To this aim, we have quantified for the first time the cell adhesion force and strength after 4 and 24 h of culture using fluid force microscopy (FluidFM). Thanks to a microfluidic cantilever that has an aperture at the free end and is connected to a pressure controller, this recently developed technique[35,38–39] allows for a strong and controlled immobilization of the cell[39,40–46] and, consequently, the quantification of adhesion forces of cells cultured on various substrates. To understand the cell adhesion behavior, the investigations further included quantification of relevant mechanical properties of the pillars and attached living cells, the morphology and cytoskeleton organization of the cells, their settling behavior on the two different patterns, FAs formation and the morphology of cell–pattern interfaces. The findings revealed new and distinctive adhesion and detachment behavior of cells after 24 h of culture on the two different patterns. The differences were explained by using adequate models. In addition, the effects of pillar height on cell adhesion properties were elucidated, and the overall results were discussed taking into account the previously demonstrated differences in the osteogenic properties of the patterns investigated in this study.

2. Results and Discussion

2.1. Morphology and Mechanical Characteristics of the Patterns

The shape, dimensions, and mechanical properties of the 3D printed submicron pillars were determined by SEM and AFM techniques (**Figure 1**).
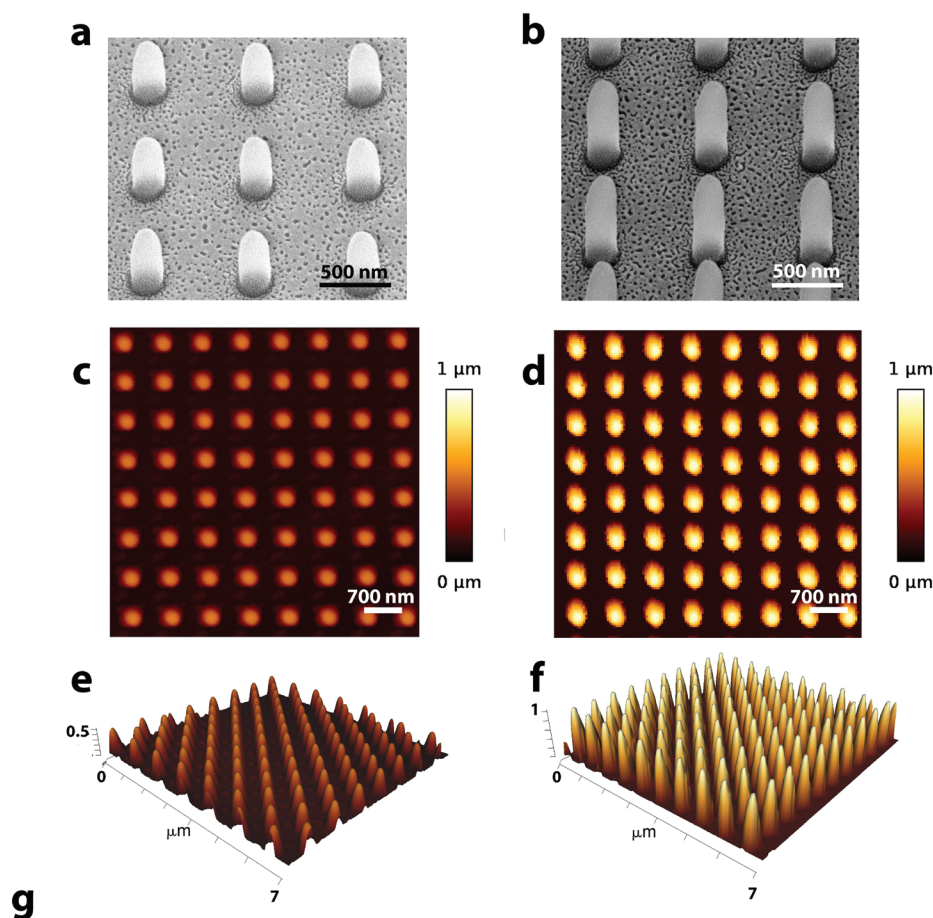
The P500 and P1000 patterns consisted of arrays of pillars with a cylindrical geometry and a round tip (Figure 1a,b). This shape is the result of the typical TPP ellipsoidal voxel shape, which is responsible for the decrease of the diameter toward the tip of the pillar.[47] The height of the round tip was estimated by SEM and found to be 150 ± 22 nm for the P500 pillars and 148 ± 16 nm for the P1000 pillars. A high consistency with the designed parameters and a high reproducibility of the height, diameter, and interspace of the printed pillars were observed by SEM (Figure 1a,b) and AFM measurements (Figure 1c–f). As measured by AFM, the average surface roughness (R_a) was 113 ± 1 and 236 ± 8.5 nm for the P500 and P1000 patterns, respectively.

During the bending tests, the pillars showed an elastic behavior over the entire range of the applied forces (Figure S1, Supporting Information). The failure of the pillars occurred because of their detachment from the substrate, without any plastic deformation or fracture of the pillar per se (Figure S1, Supporting Information). This was confirmed by the topographical images acquired after the breakage of the pillars, which revealed the absence of any material residues on the substrate (Figure S1c, Supporting Information).

The maximum stress, calculated as the maximum bending stress, was 0.32 ± 0.02 GPa for P500 pillars and 0.32 ± 0.08 GPa for P1000 pillars. Since no fracture of the pillar material was observed, this maximum stress can be considered as the adhesion strength of the pillars to the substrate, and corresponds to an adhesion force of 10 µN. The high consistency of the maximum stress found for P500 and P1000 pillars indicated that no difference in the adhesion strength was induced by the fabrication process of the pillars with the two different height values.

The average values of the pillars stiffness (k_{pillar}) were determined as 12 ± 1.0 N m^{-1} for P500 pillars and 1.3 ± 0.2 N m^{-1} for P1000 pillars, and corresponded to similar values of elastic modulus (E_{pillar}) for the two kinds of pillars (i.e., 3.4 ± 0.7 GPa for P500 and 3.3 ± 0.5 GPa for P1000, calculated assuming a cylindrical pillar). The slight difference (3.25%) between the elastic modulus values found for the two types of pillars can be ascribed to the experimental variability of the measurement method.[48] The results indicate that no changes in the intrinsic elastic properties of the polymeric material (elastic modulus) were introduced during the printing process by increasing the height of the printed pillars.

Since the diameter and the interspace of the pillars are constant parameters on P500 and P1000 samples, the stiffness of the single pillars is directly related to the effective shear modulus G of the patterned surface. The effective shear modulus was calculated as proposed by Ramussen et al.[49] and revealed a value of 6.9 ± 1.1 MPa for the P500 surface and 1.8 ± 0.7 MPa for the P1000 surface.

ADVANCED
SCIENCE NEWS
www.advancedsciencenews.com

NANO · MICRO
small
www.small-journal.com

Figure 1. Morphology of the 3D printed patterns. SEM images of the a) P500 and b) P1000 pillars; AFM 2D (c,d) and AFM 3D (e,f) topography images of P500 (c,e) and P1000 (d,f) pillars; summary of the morphological and mechanical parameters of the individual submicron pillars and the patterned surfaces (g).

Parameter	P500	P1000
Pillar height (h_{pillar}) [nm]	461 ± 63	1034 ± 30.5
Pillar diameter (D_{pillar}) [nm]	205 ± 10	199 ± 10
Pillar interspace (I) [nm]	702 ± 17	693 ± 24
Surface roughness (R_a) [nm]	113 ± 1	236 ± 8.5
Pillar stiffness (k_{pillar}) [N/m]	12 ± 1.0	1.3 ± 0.2
Pillar elastic modulus (E_{pillar}) [GPa]	3.4 ± 0.7	3.3 ± 0.5
Pillar maximum lateral force ($F_{N,xy,max}$) [nN]	744 ± 46	364 ± 96
Pillar maximum displacement ($d_{pillar,max}$) [nm]	61 ± 9	289 ± 85
Pillar adhesion strength to the substrate (σ_{max}) [GPa]	0.32 ± 0.02	0.32 ± 0.08
Surface effective shear modulus (G) [MPa]	6.9 ± 1.1	1.8 ± 0.7

2.2. Cell Adhesion

2.2.1. General Observations during the FluidFM Experiments

For all the tested cells (on all substrates at both 4 and 24 h), the failure of the cell–substrate contact (points 3 in **Figure 2**a,c,e) occurred in a small region underneath the probe. Indeed, no changes in the morphology at the periphery of the cells were observed by optical microscopy (Figure 2b-4,d-4,f-4) when the peak force (points 3 in Figure 2a,c,e) was recorded.

After the first detachment (corresponding to the peak force), the measured force decreased, with a trend characterized by discrete steps, ascribable to cell detachment events, as widely reported in the literature.[33] The measured force reached in general a very low value, close to zero, (point 4 of Figure 2a,c) when the peripheral parts of the cell were still attached to the surface. Since only the vertical component of the force is detected in FluidFM measurements, this means that those peripheral parts were subjected to negligible vertical components of the force. The observed behavior is consistent with the fact that, in
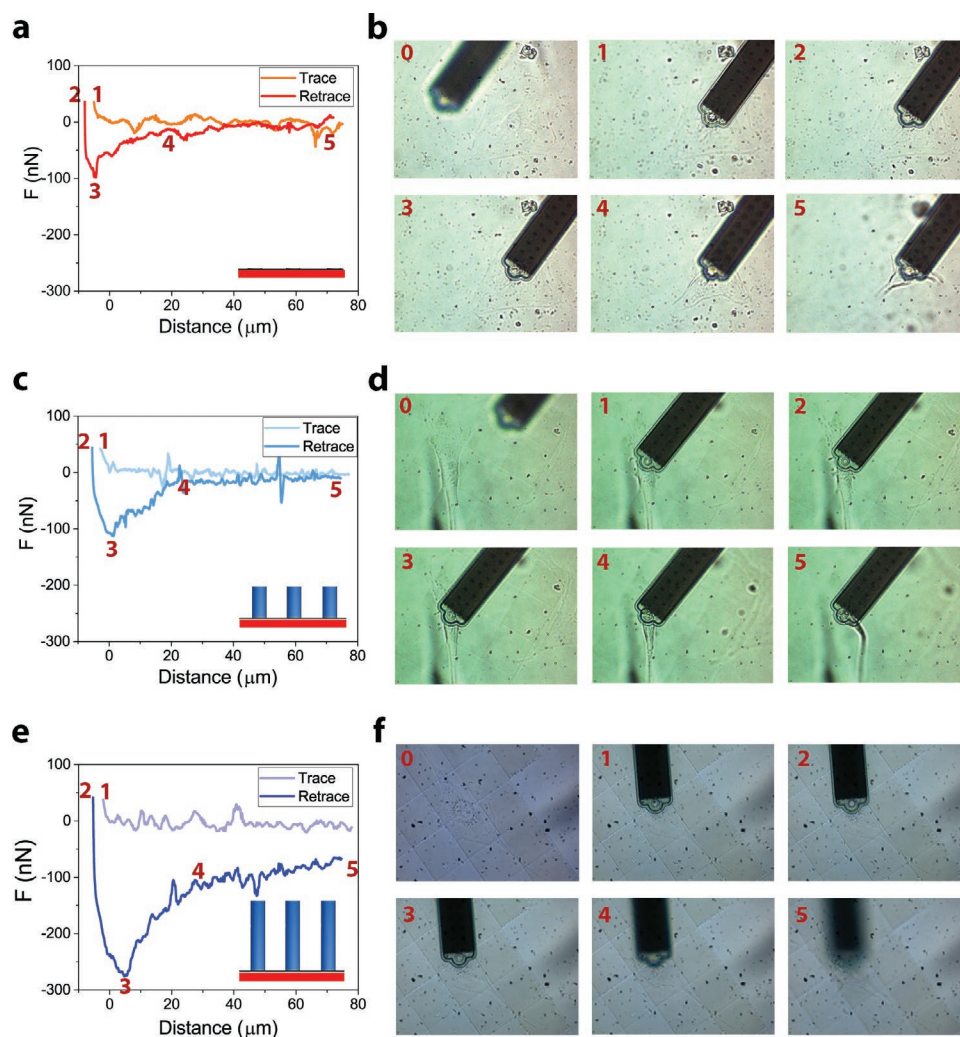
ADVANCED
SCIENCE NEWS
www.advancedsciencenews.com

NANO · MICRO
small
www.small-journal.com

Figure 2. Representative results of the FluidFM experiments after 24 h of MC3T3-E1 preosteoblast cell culture: a,c,e) force–distance curves obtained on the flat glass control surface (a), the P500 (c) and the P1000 (e) patterns; b,d,f) optical images of the cell morphology at the different phases of the experiments: 0) before starting the experiments; 1) when the cell was approached with a predefined setpoint force (50 nN); 2) at the beginning of the probe retraction (i.e., at the end of the pause in force constant mode, during which the under pressure was applied to grab the cell); 3) when the failure of the cell–surface contact was observed (i.e., the peak force was recorded); 4) at the beginning of the force plateau; and 5) at the end of the experiment (when a distance of 80 μm was reached). The videos corresponding to the reported example experiments are available in SV1–SV3, Supporting Information.

the FluidFM experiments, the force is locally applied to the cell surface at a point corresponding to the probe's aperture, that is, the region above the nucleus.

This detachment behavior can be explained by considering the cell discretized in a set of straight elastic fibers (i.e., springs), connecting the center of the aperture of the probe with an area (sufficiently small) of the cell–substrate contact surface (**Figure 3**a). The total measured vertical force can be written as:

$$F_{z,tot} = \sum_i F_{z,i} = E \frac{\Delta H}{H} \sum_i A_i \sin^4 \alpha_i \qquad (1)$$

where $F_{z,i} = E \frac{\Delta H}{H} A_i \sin^4 \alpha_i$ is the vertical component of the force applied to the element of the cell–substrate contact area of area A_i (Figure 3a). E is the elastic modulus of the single fiber (meaning the elastic constant per unit length per unit area), which we considered equal for all the fibers. H is the initial height of the cell, and ΔH is the probe's elevation (height variation) when it is retracted (Figure 3a). α_i is the inclination angle of the generic ith fiber (Figure 3a). The derivation of Equation (2) is reported in Section S3, Supporting Information.

According to this model, $F_{z,i}$ is maximum for $\alpha_i = 90°$, that is, the point right under the probe's aperture, and rapidly decreases with the angle α, that is, the distance between the probe's aperture and the anchoring point of the single fiber to the surface.

Although this is a simplified model, it represents well the experimental observations. Indeed, it shows that the area of the cell under the tip is the most loaded and explains why, in all our experiments, the first region of the cell to be detached was the central region. On the contrary, the peripheral parts, being far from the aperture of the probe (point of application of the force), were subjected to negligible vertical components and large in-plane (horizontal) components of the applied forces.
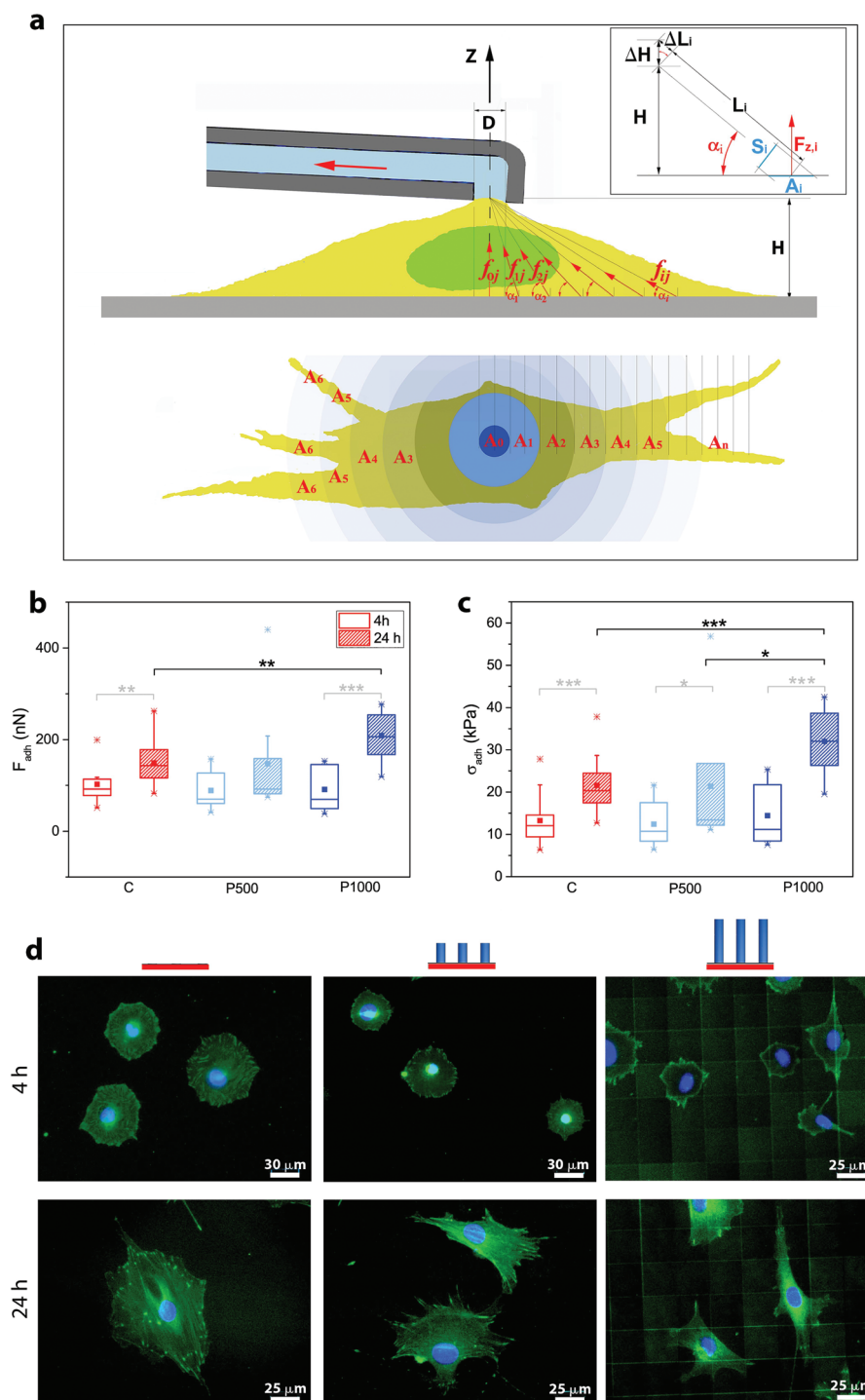
Figure 3. a) Schematics of the model describing the cell detachment in FluidFM experiments. The cell was considered to consist of straight elastic fibers with orthogonal section s_{ij} connecting the point of application of the force (center of the probe's aperture of diameter D) with a point (ij) of the cell–substrate contact area. α_i is the inclination angle of the generic fiber. The cell–substrate contact area was discretized in i circular crowns (or segments of circular crowns) with area $A_i = \dfrac{S_i}{\sin \alpha_i} = \dfrac{\sum_j s_{ij}}{\sin \alpha_i}$ and center corresponding to the point of application of the force. f_{ij} is the traction forces acting along the single ijth fiber when the probe is retracted. H is the (initial) height of the cell at the point of application of the force. L_i is the (initial) length of the generic fiber and ΔL_i is the fiber's elongation when the probe is retracted of ΔH. $F_{z,i}$ is the ith contribution to the total measured force. b,c) Quantitative characterization of cell adhesion (b) and cell adhesion strength (σ_{adh}) (c). Empty boxes represent data after 4 h and striped boxes after 24 h of cell culture on the glass substrate (control) and the P500 and P1000 patterns. A one-way ANOVA test followed by Tukey's multiple pairwise comparisons post hoc test was used to evaluate the statistical significance of the differences between the various experimental groups (* $p < 0.1$, ** $p < 0.05$, *** $p < 0.01$). d) Vinculin staining of the cells cultured on the control, the P500 and P1000 patterns after 4 and 24 h.

This was supported by the optical microscopy images acquired during the probe retraction revealing that the cell's periphery slid in the direction of the point of application of the force under the action of the in-plane components of the force and, only in the end, entirely detached from the surface (Figure 2b-6,d-6). This was confirmed also by optical microscopy images of partially detached cells (Section S3, Supporting Information), where only the central region under the probe's aperture was detached. It is worth noting that since the FluidFM measurements are based on detecting the sole vertical deflection of the cantilever, the in-plane forces are not detected, and quantitative information about the cell resistance to shear forces cannot be retrieved.

However, qualitatively, the cells cultured on the different substrates exhibited a different behavior at the periphery during the detachment, which can be attributed to a different resistance to shear forces. In the case of cells cultured on glass (control substrate) and P500 pattern, the measured vertical force reached a small, almost zero and constant value at a probe retraction distance of ≈20 µm (point 4 of Figure 2a,c), indicating that the central part of the cell was completely detached. Continuing the retraction of the probe, the peripheral regions of the cells slid toward the center (point of application of the force) and detached (Figure 2b-6 to 2d,c). On the contrary, cells cultured on the P1000 pattern for 4 and 24 h were not entirely detached in most of our experiments. Peripheral parts of the cell were often constrained and could not slide on the surface toward the point of application of the force (Figure 2f-6).

This indicates a positive effect of the P1000 pattern on the anchoring of the cells, which seems to resist shear (in-plane) forces better than the cells cultured on the other substrates (P500 pattern and the flat control surface). However, as mentioned above, the higher resistance to shear forces of the cells attached to the P1000 surface was observed only qualitatively since the FluidFM measurements do not provide any quantitative information about the horizontal components of the applied forces.

This stronger attachment of the cells to the P1000 pattern was also observed in the recorded force–distance curves, where, often, the final value of the (vertical) force was higher than the one recorded on the P500 and the flat control surfaces (Figure 2e, point 5), that is, the retraction curve did not reach the baseline of the approach curve.

2.2.2. Adhesion Force

Even if the cells were not completely detached from the P1000 surfaces, it was possible to quantify the adhesion force of the cells to all the surfaces (Figure 3b). The adhesion force is defined as the difference between the peak force and the baseline, that is, the zero-force level of the approach curve. Indeed, the adhesion force is the maximum force required to detach the most loaded region of the cell. Therefore, it is unnecessary to detach the entire cell to retrieve this cell–surface adhesion force value. The measured values of adhesion force were in the range 20–300 nN, which are two-three orders of magnitude lower than the adhesion force of the pillars to the substrate (10 µN). This means that the pillars could not be detached by the application of the forces used in FluidFM experiment and confirms the detachment of the cells from the pillars.

After 4 h of cell culture, no significant difference was observed in the adhesion force of the cells cultured on the different substrates (i.e., 102 ± 43 nN on the control flat glass surface, 89 ± 40 nN on P500, and 91 ± 46 nN on P1000). Increasing the cell culture time (from 4 to 24 h), the cell adhesion force increased on all the substrates. The increase was ≈50% on the flat control surface and the P500 pattern, while an increase of nearly 100% was observed on the P1000 pattern. The cell adhesion force after 24 h was significantly higher (209 ± 54 nN) on the pattern characterized by the tallest pillars, that is, P1000, than the flat control surface (149 ± 54 nN). On the contrary, the P500 pattern exhibited an average value of cell adhesion similar to the flat substrate (157 ± 133 nN). This indicates that the height of the pillars had a significant influence on cell adhesion after 24 h of cell culture.

However, due to the high variability of the cell shape and size observed on the different surfaces (Figure 2b-1,d-1,f-1) and at the different tested incubation times, the values of the measured adhesion force cannot be directly compared, especially considering that, in FluidFM experiments, the force is locally applied on the cell in an area corresponding to the position of the probe aperture. Therefore, the cell's different regions are strained depending on the distance to the application point of the force.

2.2.3. Adhesion Strength

To compare the quantitative data acquired on different surfaces and after different cell culture durations, we estimated the adhesion strength of the cells cultured on the different substrates after 4 and 24 h (Figure 3c) as:

$$\sigma_{max} = E\frac{\Delta H}{H} = \frac{F_{z,tot}}{\sum_i A_i \sin^4 \alpha_i} \tag{2}$$

Details about the derivation of the equation for the cell adhesion strength (maximum stress) are reported in Section S3, Supporting Information.

After 4 h of cell culture, the patterns did not affect the cell adhesion strength. Indeed, the cells cultured on all the surfaces showed no difference in the adhesion strength values.

By increasing the cell culture time (from 4 to 24 h), the increase in cell adhesion strength was observed on all the substrates (flat control surface, P500, and P1000), coherent with the expected strengthening of cell–surface adhesion. Indeed, the initial attachment of cells to a substrate is driven by integrin-mediated interactions and consists of binding single receptor-ligand pairs.[36,50,51] After this initial attachment, cells spread on the substrate, increasing the contact area, reorganizing the actin cytoskeleton, forming focal adhesions and increasing the adhesion strength.[36,52,53]

After 24 h, the cells on the P1000 exhibited significantly higher adhesion strength than on the flat control surface and P500 pattern. Furthermore, the cells cultured for 24 h on the P500 pattern showed a cell adhesion behavior similar to the flat glass. These results indicate a different mechanism of interaction of the cells with the tallest pillars (height of 1000 nm), which makes the cells more firmly attached to the surface and more resistant to "out of plane" forces after 24 h of incubation.

The measured adhesion strength of cells interacting with submicron patterns, quantified for the first time by FluidFM in this study, is coherent with previous qualitative results on random and controlled surface roughness in the submicron range, where the cell adhesion was enhanced with the increase of the surface roughness.[9,49,54–57]

2.2.4. Formation of Focal Adhesions

After 4 h of cell culture, we observed the formation of vinculin rich sites at the periphery of the cells cultured on all the surfaces. They were mainly nascent vinculin sites in the cells cultured on the flat control surface and the P500 pattern, while membrane extensions rich in vinculin were already observed on the P1000 pattern (Figure 3d). This suggests a stronger interaction of the cells with the P1000 pattern and the start of FAs maturation at the periphery of the cells after 4 h. However, the FluidFM measurements after 4 h did not show any significant difference in the quantitative value of cell adhesion force and strength. This apparent contradiction can be ascribed to the fact that the measurement of the adhesion strength by FluidFM is local and, in our case, expressed relative to the cell's central (nuclear) region. Therefore, possible differences in the adhesion at the periphery of the cells (e.g., a stronger attachment of the cells on the P1000 pattern) could not be quantitatively detected by FluidFM under our experimental conditions. However, a higher shear resistance of cells on the P1000 pattern was qualitatively observed after 4 h (Figure 2) which is in line with the presence of many sites rich in vinculin at the periphery.

After 24 h, FAs were present in cells cultured on all the substrates. Qualitatively, FAs' area and density increased in the cells cultured on the patterns compared to the cells on the flat control surface, but were similar on the P500 and the P1000 patterns (Figure 3d). It is worth noting that a precise quantification of FAs' area and density was not possible because of the 3D topography of the surfaces and the limited size of the pillars, even below the resolution limit of z-stack confocal microscopy.

The similar FAs' size, density and distribution on the two patterns after 24 h of cell culture indicate that the reinforcement of cell adhesion on the P1000 arrays is not related to a difference in the FAs formation but could be determined by the physical cell–surface interactions, for example, the cell settling state on the taller pillars.

2.3. Cell–Pattern Interface

A SEM analysis of the surface–pattern interfaces (**Figure 4**a–d,f–j) revealed that cells adhered on the top and the sidewalls ("middle" state) of the pillars, or on the top, the sidewalls, and the substrate ("bottom" state).[58] More specifically, the cells cultured for 24 h on the P1000 pattern exhibited a "middle" settling state in all the visible regions (both at the periphery and in the center), that is, the cells adhered on the top of the pillars and partially on their sidewalls, without coming into contact with the flat substrate (Figure 4f-1). By comparison, cells cultured for 24 h on the P500 pattern exhibited a dominant "bottom" settling state with most of cell areas in which

the cell membrane completely engulfing the pillars and coming into contact also with the flat substrate between them (Figure 4a–d). Only limited portions at the periphery of the cells exhibited a "middle" settling state on P500 pattern. On the P1000 pattern, the cell adhesion depth l_{adh} (i.e., the depth corresponding to the portion of the sidewall of the pillar to which the cell membrane adheres) was quantified and resulted in a value of 363 ± 136 nm. Similar values of adhesion depth were measured on the P500 pattern: 378 ± 78 nm in the (limited) regions characterized by the "middle" state and 500 nm (i.e., the height of the pillars) in the regions characterized by the "bottom" state.

The similar adhesion depth found for the two patterns is in line with previous studies, where the cell adhesion depth on the pillar arrays demonstrated to be mainly dependent on the material type, the diameter of the pillars and the spatial density of the pillars,[58,59] all of which are constant in our P500 and P1000 patterns. Using the measured adhesion depth value and considering the repeating unit of the pattern, we calculated the effective cell–pattern contact area on the P1000 surface as $A_{cell-P1000} = \pi R^2_{pillar} + 2\pi R_{pillar} l_{adh}$, which resulted in being ≈ 53% of the cell–glass (flat) contact area. Thus, even though the total surface area is increased by patterning the surface, the effective cell–surface contact area on the P1000 pattern significantly decreased compared to the flat surface. Therefore, the adhesion strength and the total surface area do not correlate, as also shown in previous studies.[54,60]

Being not related to the contact area nor to the FAs size and/or distribution (that were similar in both patterns), we hypothesize that the increased cell adhesion on the P1000 samples as compared to the glass and the P500 can be only ascribed to the contribution of the parts of the cells adhering on the sidewalls of the pillars. Indeed, when a normal (vertical) force is applied to the cells attached to the pillars, those regions adhering to the sidewalls are subjected to shear stress (τ) and, therefore, need a higher vertical (out-of-plane) force to be detached as compared to the cell regions subjected to a normal stress σ (i.e., adhering on the flat surface).[61]

However, since the cell adhesion strength on the P500 pattern was lower than the P1000 (and similar to that one measured on the flat control surface), our experimental (FluidFM) data seems to indicate that when part of the cells also adhere on the substrate between the pillars, the contribution of the parts of the cell adhering on sidewalls becomes negligible. To explain this finding, let us consider a generic element of the cell between two pillars (Figure 4k,l) subjected to vertical stress (σ_z). When the cell is adherent to the substrate (Figure 4k), the element is subjected to traction and it elongates and tends to undergo lateral contraction. The lateral contraction is hindered by contact with the sidewall of the pillars. Therefore, there is a reaction force (normal to the lateral surface of the pillar) which, in addition to the applied shear stress, can tend to detach the cell from the pillar's surface, reducing its capability to adhere to the pillars' sidewalls (Figure 4k,m).

On the contrary, when the cell does not adhere to the bottom (Figure 4l), the generic element experiences no traction: it undergoes a displacement without elongation. The element does not tend to contract, and there is no reaction force normal to the sidewall of the pillar (Figure 4l). In addition, in the absence of traction, only the elements near the lateral surface of the pillar are in tension (along z), as they are (tangentially)
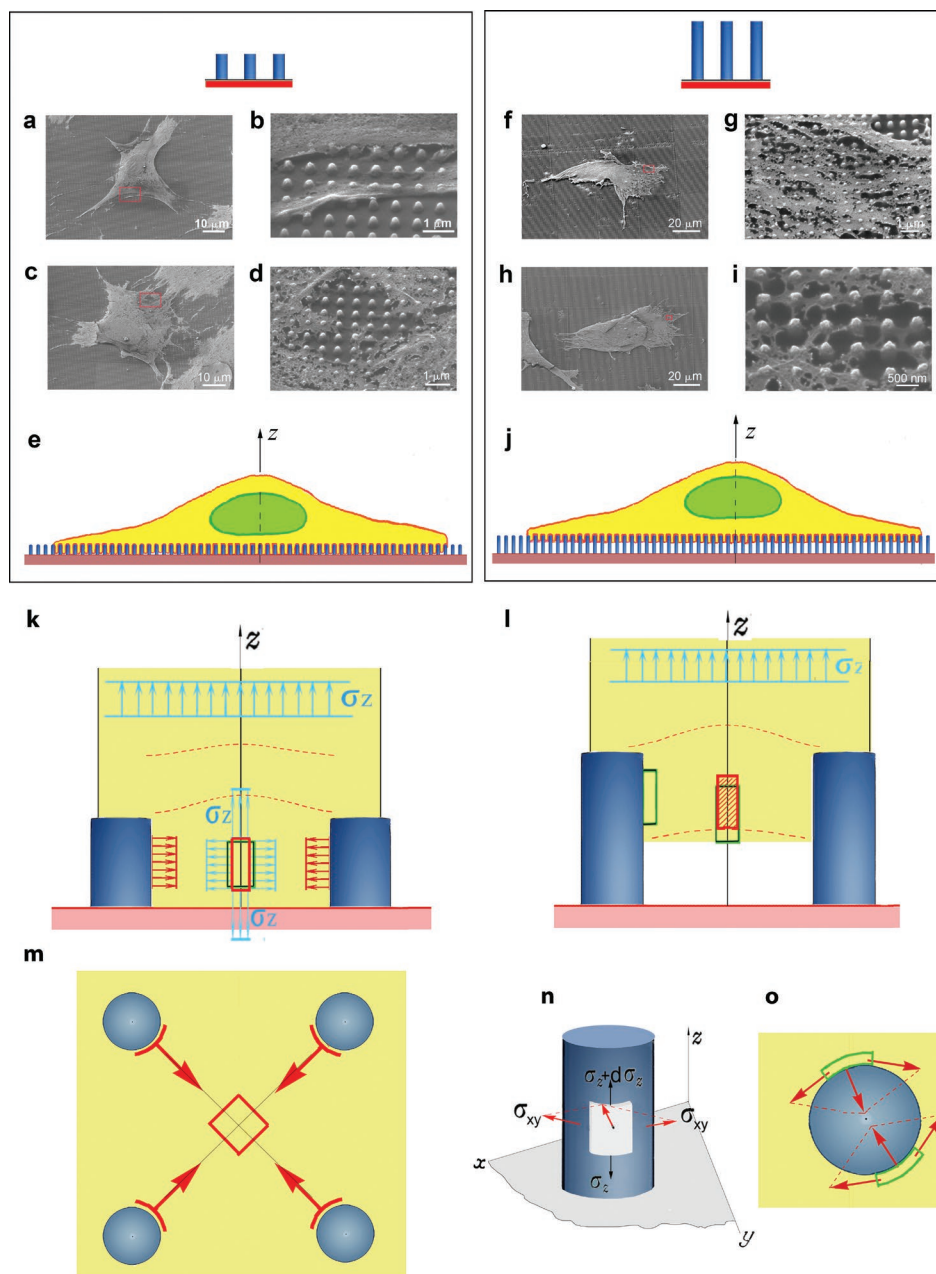
**ADVANCED
SCIENCE NEWS**

www.advancedsciencenews.com

**NANO · MICRO
small**

www.small-journal.com

Figure 4. SEM images of the MC3T3-E1 cells interacting with a–d) P500 pattern and f–i) P1000 pattern. The red squares in the low resolution images (a,c,f,h) represent the locations of the high resolution images (b,d,g,i). Schematics of the cell settling state observed on the different patterns: e) a "bottom" settling state on the P500 pattern and j) a "middle" settling state on the P1000 pattern. k–o) Lateral view (k,l,n) and top view (m,o) of a generic element of the cell between two pillars subjected to vertical stress (σ_z). In the case the cell touches the substrate (k,m), the element elongates and tends to undergo lateral contraction. As a consequence, there is a reaction force normal to the sidewalls of the pillars. In the case the cell does not touch the substrate (l,n,o), the element undergoes a displacement without elongation and there is no reaction force at the sidewall of the pillar. The elements near the sidewall of the pillars are in tension, since they are held by the surface of the pillars (o), and tend to undergo lateral contraction, producing an increase of the lateral pressure on the sidewall of the pillar.

held by the surface of the pillar (shear) (Figure 4n). Therefore, only these elements near the pillars' sidewalls tend to undergo lateral contraction, producing a consistent increase in the pressure on the lateral cylindrical surface of the pillar, as schematically shown in Figure 4n,o.

It is worth noting that, due to the cell fixation and dehydration process (SEM sample preparation), there could be a cell

volume decrease which might result in forces that pull the cell upward. However, the fact that on P500 we observed a dominant bottom state in SEM images indicates that the stress due to dehydration is lower than the adhesion strength of the cell to the substrate. Therefore, it cannot change the cell settling state on the P500 pattern. In the case of the cells characterized by a "middle state," that is, the cells cultured on the P1000 pattern,

**ADVANCED
SCIENCE NEWS**

www.advancedsciencenews.com

**NANO · MICRO
small**

www.small-journal.com

the suspended region (i.e., the portion of the cell membrane between the pillars) could go up during dehydration, but the (shear) stress needed to detach the cell membrane from the sidewall of the pillars should be even higher than the stress required to detach the cell from the substrate. Since the value of cell adhesion depth on the P1000 pattern was measured on the cell parts adhering to the sidewalls of the pillars, it cannot be significantly affected by the dehydration process.

Therefore, the SEM analysis of the interface between the patterns and the cells after 24 h of cell culture indicates that the increase of the cell adhesion strength to the P1000 surface can be ascribed to the way cells interact and settle onto the pattern: the cells characterized by a "middle state" partially adhere to the sidewalls of the pillars, increasing their resistance to forces applied normally to the surface.

2.4. Morphology and Mechanics of Living Cells Attached to the Patterns

Consistent with our previous immunostaining and SEM analyses on similar surfaces,[14,29] three different cell shapes were observed by AFM imaging of live cells on the different surfaces (**Figure 5**a): i) polygonal cells, with the contour similar to a polygonal chain with 4 to 6 vertices and a low degree of anisotropy (aspect ratio, i.e., the ratio between the major and the minor axis of the cells, < 2); ii) stellate cells, characterized by multidirectional membrane extensions (e.g., filopodia); and iii) elongated (polarized) cells, with a visible main direction of elongation and a high degree of anisotropy (aspect ratio > 2).

Polygonal cells were mostly observed on the flat substrate (Figure 5b). They often presented wider leading edges, suggesting a motile behavior,[62] after both 4 (Figure 5a-1) and 24 h of cell culture (Figure 5a-7). Stellate cells were not observed on the flat surface but made up ≈50% of the cells on both P500 and P1000 specimens after 4 and 24 h of cell culture. Stellate cells after 4 h on both P500 (Figure 4a-3) and P1000 (Figure 5a-5) surfaces were rather symmetric and did not show a morphology ascribable to a motile behavior. After 24 h, most of the stellate cells exhibited wider leading edges, indicating a possible motile behavior (Figure 5a-9,11). Interestingly, we observed that the membrane extensions of stellate cells on both patterns and at both cell culture times (4 and 24 h) were directed along with repetitive directions, which corresponded to the main directions of the arrays (e.g., 0°, 26.56°, 45°, 90°), as shown in **Figure 6**. AFM high-resolution images of the cell membrane protrusions (Figure 6b,1–3) revealed that filopodia tend to extend on the top of the pillars or inside the channels between them, adhering to the sidewalls of the pillars, as it was mainly observed on P1000 samples (Figure 6b-1), or on the substrate between them, as mainly observed on P500 samples (Figure 6b-2,3). This contact guidance effect of the pillar arrays on membrane protrusions appears responsible for spreading the cells along specific preferred directions.

Elongated cells were present on all the surfaces after 4 and 24 h of cell culture. They made up ≈30% of the total cells on the flat surface after 4 h and 40% after 24 h. On both P500 and P1000 patterns, elongated cells were 50% of the total cells after 4 and 24 h. The elongated cells on the patterns exhibited a higher aspect ratio than the elongated cells observed on the flat surface. Their major axis was always directed along one of the main directions of the pillar arrays (Figure 5a-4,6,10,12). This confirms the capability of patterned surfaces to promote cell spreading preferentially along the main directions of the array, as similarly observed for stellate cells.

Quantification of cell area (Figure 5c) indicated that after 4 h of culture, cells on the patterns exhibited a smaller area than the ones on the flat surface. No significant difference was observed between the cell area on P500 and P1000 patterns. With the increase in the cell culture time (from 4 to 24 h), the cell area increased on the flat and P500 surfaces. By comparison, cells on the P1000 pattern did not show any increase in the cell area after 24 h resulting in significantly smaller areas compared to the cells on the P500 and flat surfaces. This effect appears to be related to cells adhesion and settling behavior onto the patterns. The taller pillars (P1000), on which the cells exhibited a "middle" settling state, seem to act not only as anchoring points improving the cell adhesion and the cell resistance to shear forces but also as obstacles limiting the capability of cells to spread onto the substrate. The average height of the cells was significantly higher on the patterns than the flat control after both 4 and 24 h (Figure 5d) reflecting the effects of the patterns on cell spreading.

However, the maximum height of the cells, that is, the height corresponding to the top of the nucleus, was similar for the cells cultured on all the substrates at both 4 and 24 h of cell culture (Figure 5d), suggesting that the interaction with the different substrates did not produce any significant effect on the shape of the nucleus (Figure 5e). However, no information about the lateral size and shape of the nuclei could be retrieved from the AFM data.

For cytoskeleton organization, high-resolution images of the actin cytoskeleton organization were obtained by reconstructing the live cells mechanical (elastic modulus) maps (**Figure 7**). We have used orientation coherency as a quantitative parameter describing the orientation of the actin fibers in the region above the nucleus.

On the flat control surfaces, after 4 h (Figure 7a-1,2), both polygonal and polarized cells exhibited the presence of numerous and thick peripheral fibers, directed approximately parallel to the sides of the cells. Differently, the region above the nucleus was characterized by few, almost aligned, actin fibers, crossing the cells from the leading edge to the rear, suggesting a motile state, where, in general, the actin fibers tend to align in the direction of the movement. This cytoskeleton organization gave rise to an orientation coherency of 0.34 ± 0.07 (Figure 7b). With the increase of the cell culture time, that is, after 24 h, we (qualitatively) observed the thickening of actin fibers both in the peripheral regions and above the nucleus for the polygonal and elongated cells (Figure 7a-7,8). In addition, less fibers were visible after 24 h in the region above the nucleus but they were thicker and more aligned. This significantly increased the orientation coherency measured in this region (Figure 7b).

A closer look at the cytoskeleton organization revealed differences between the flat and patterned surfaces. After 4 h of cell culture, both stellate and elongated cells on the patterns were characterized by peripheral and ventral actin fibers.
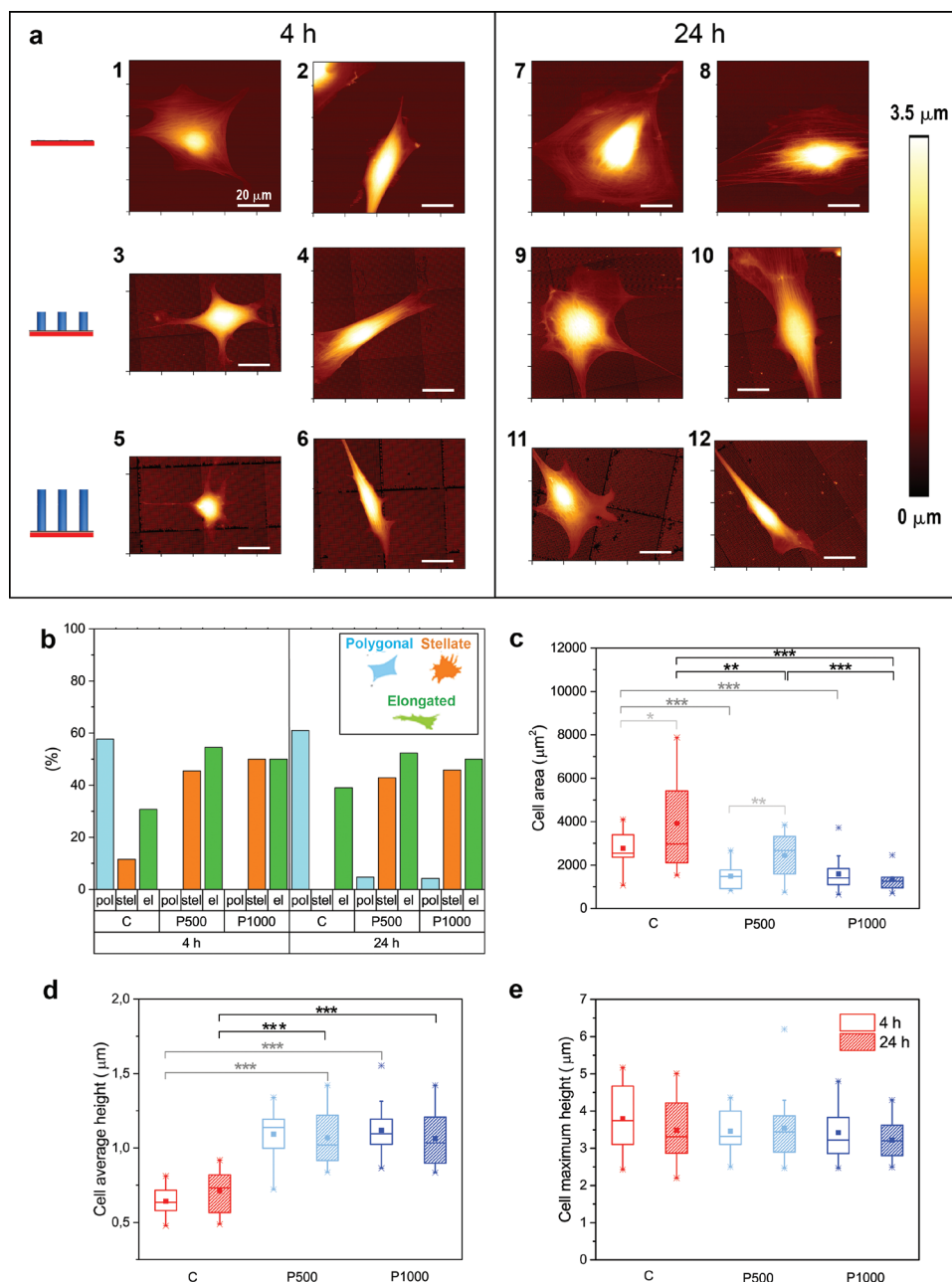
ADVANCED
SCIENCE NEWS
www.advancedsciencenews.com

NANO · MICRO
small
www.small-journal.com

Figure 5. Morphological analysis of cells by AFM QI mode: a) representative topography images of MC3T3-E1 cells interacting with the flat glass control (top row), P500 (middle row) and P1000 (bottom row) patterned surfaces, after 4 (1–6) and 24 h (7–12) of cell culture. b) The percentage of the different observed types of the morphology of the cells (polygonal, stellate, and elongated) on the control and the patterned surfaces, after 4 and 24 h of cell culture; c) the cell–substrate contact area, d) the average height and e) the maximum height, measured at the highest point of the region above the nucleus, of MC3T3-E1 cells on the flat control, the P500, and P1000 surfaces after 4 (empty boxes) and 24 h (striped boxes) of cell culture. The one-way ANOVA test followed by Tukey's multiple pairwise comparisons post hoc test was used to evaluate the statistical significance of the differences between the various experimental groups (* $p < 0.1$, ** $p < 0.05$, *** $p < 0.01$).

The actin fibers were stretched in all directions in stellate cells (Figure 7a-3) and directed along the major axis in the elongated cells (Figure 7a-4). Significantly few thin fibers were observed in the region above the nucleus in both cell morphologies (Figure 7a-3,4) after 4 h, resulting in a low orientation coherency in this region (Figure 7b). After 24 h of cell culture, stellate cells exhibited a particular cytoskeletal organization in the region above the nucleus consisting of a complex network of

actin fibers directed along different directions. Fibers crossing this region were also observed on polarized cells, which mainly aligned along the direction of the cell's major axis. From a quantitative point of view, the orientation coherency in the region above the nucleus increased with the cell culture time (Figure 7b). Still, it was significantly lower than in the cells cultured on the glass surfaces. This was due to the network-like orientation of the fibers of the stellate cells, which made
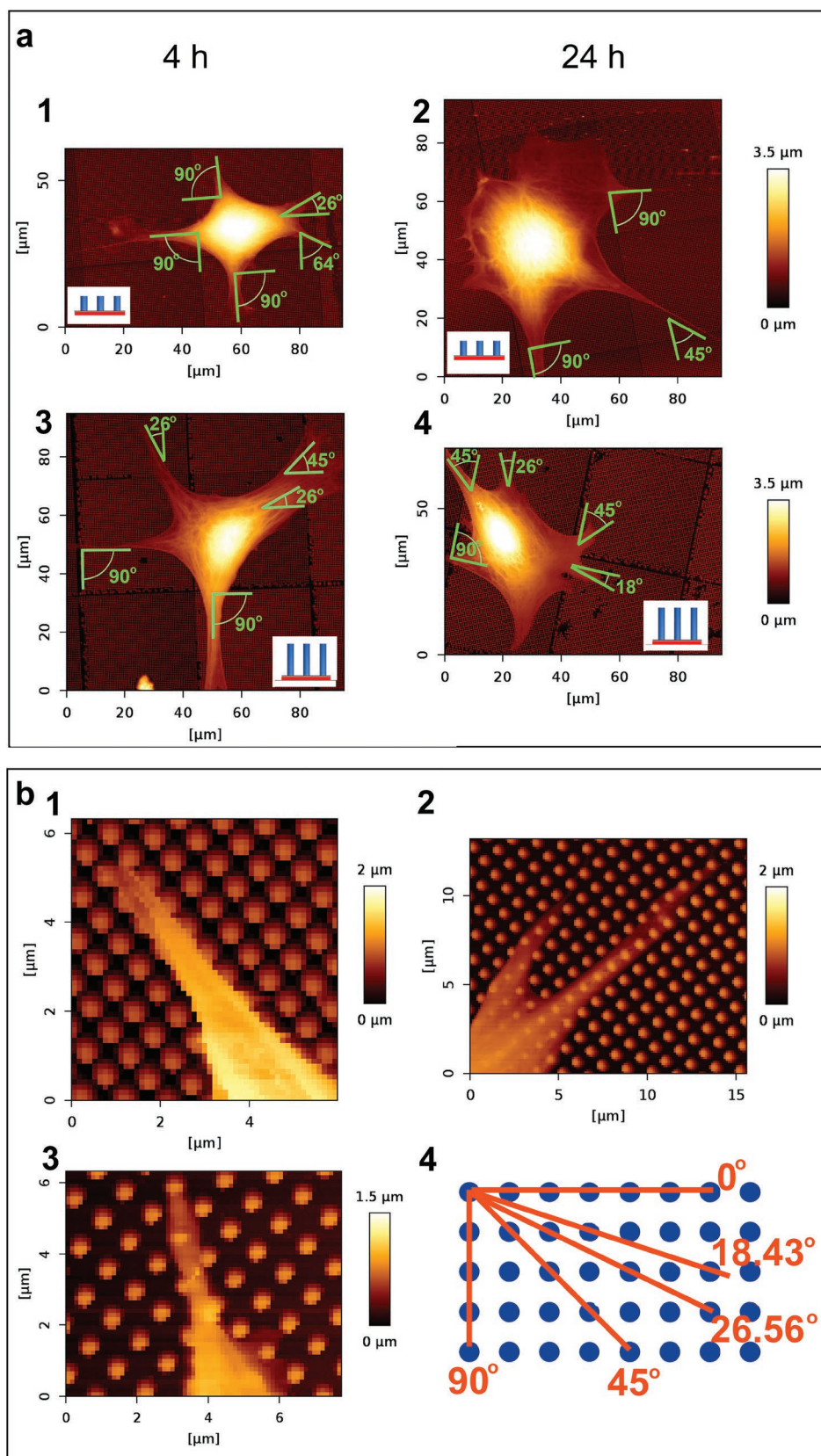
Figure 6. Preferential spreading directions of cells on the patterned surfaces: a) representative AFM topography images of the directions of the cell membrane extensions on P500 (1,2) and P1000 (3,4) patterned surfaces. b) Details on the attachment of the membrane extension on the P1000 (1) and P500 (2,3) patterns and schematics of the observed preferential directions of the membrane protrusions (0°, 26.56°, 45°, 90°) (4).
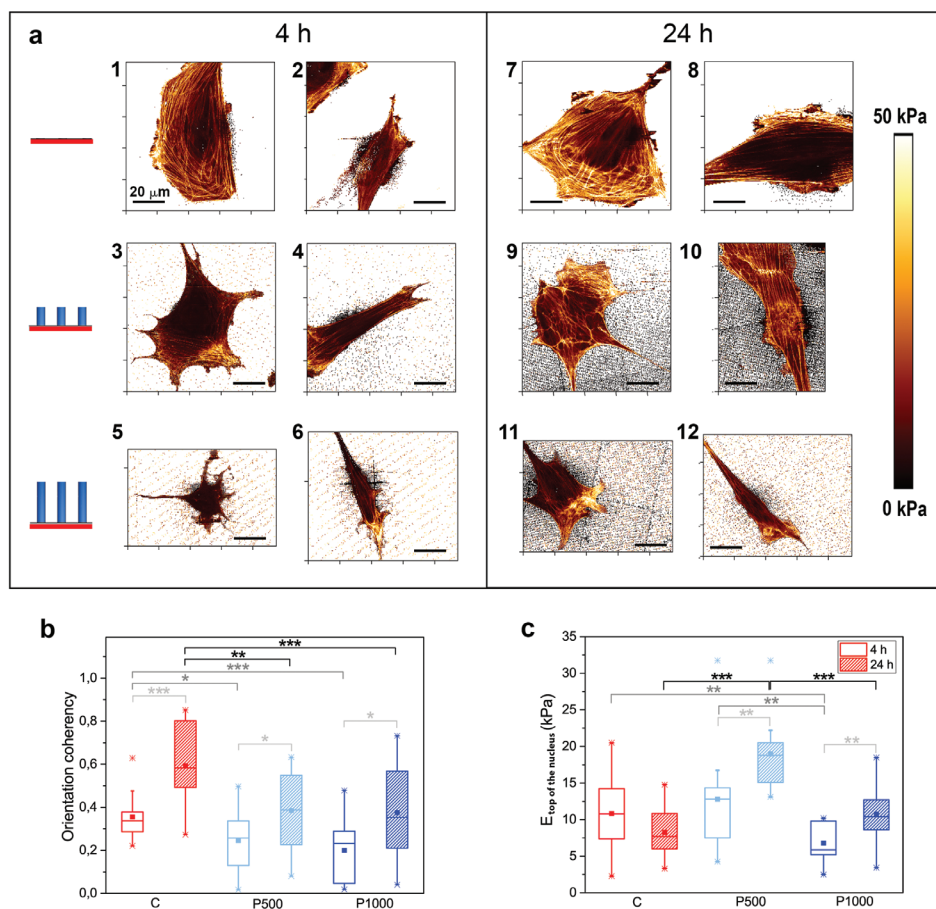
Figure 7. Elastic modulus (EM) mapping of the cells by AFM QI mode: a) representative EM maps of MC3T3-E1 cells residing on the flat glass (top row), the P500 (middle row) and P1000 (bottom row) patterned surfaces, after 4 (1–6) and 24 h (7–12) of cell culture. b) The orientation coherency and c) the average elastic modulus measured in the region above the nucleus of the cells residing on the flat control, the P500 and P1000 surfaces after 4 (empty boxes) and 24 h (striped boxes) of cell culture. The one-way ANOVA test followed by Tukey's multiple pairwise comparisons post hoc test was used to evaluate the statistical significance of the differences between the various experimental groups (* $p < 0.1$, ** $p < 0.05$, *** $p < 0.01$). Note that the difference in the color of the substrate has no physical meaning in this case and should be ignored.

up ≈50% of the cells residing on the patterns. Since stress fibers tend to align in the direction of the exerted mechanical forces,[63,64] this could indicate that stellate cells cultured on the patterns are subjected to isometric tension, that is, forces directed in all directions.

Although the orientation of the actin fibers in the regions above the nucleus was similar in cells cultured on the P500 and P1000 patterns, the fibers thickness was different. Thick bundles of actin fibers mainly characterized cells cultured on the P500 pattern. In some cells, we also observed the presence of actin star sites (e.g., Figure 7a-9), indicating the entanglement of several multidirectional actin bundles.[65,66] This kind of branched cytoskeleton, characterized by a network-like distribution of stress fibers and the presence of actin patterns, has been previously associated with high levels of intrinsic mechanical stress within the actin network.[14,67–69] On the contrary, the actin fibers observed in the regions above the nucleus of the cells cultured on the P1000 patterns were thinner and less polymerized.

Consequently, cells on P500 and P1000 patterns exhibited different values of elastic modulus measured in the region

above the nucleus (Figure 7c). Namely, after 4 and 24 h of cell culture, cells on the P500 patterns exhibited significantly higher elastic modulus than those cultured on the P1000. The elastic modulus of the region above the nucleus of cells cultured on the flat glass surface was lower than that of the cells on the P500 because of the different distribution of the fibers, which were mainly located at the periphery and the base of the cells, and not crossing above the nucleus. It is worth noting that the reported values of elastic modulus are not relevant for the overall cell but only for the region above the nucleus.

A highly polymerized cytoskeleton and a high elastic modulus were previously associated with a high tension exerted on the cells.[14,67–69] Also, tension and stretching can promote the thickening of the stress fibers along the direction of the applied forces.[63,64] According to that, we could conclude that cells cultured for 24 h on the P500 pattern are subjected to a higher tension than those cultured on the P1000 surface. However, it is worth noting that the relationship between the actin cytoskeleton development and the intensity of the exerted forces is not straightforward. Different cell responses to tension and stretching can occur, for example: i) monotonic

ADVANCED
SCIENCE NEWS
www.advancedsciencenews.com

NANO · MICRO
small
www.small-journal.com

reinforcement, including the growth of stress fibers, but also; ii) retraction, that is, depolymerization of stress fibers with consequent softening and fluidification of the cells; and iii) reinforcement after retraction.[70,71] This means that actin filaments in stress fibers may undergo polymerization or depolymerization while sustaining high tensile forces. Therefore, our characterization, consisting of the sole observation of actin stress fibers orientation and the quantification of the local elastic modulus in the regions above the nucleus, cannot furnish direct and univocal quantitative information about the magnitude of the intracellular tensions that should be further investigated with other methods, such as traction force microscopy (TFM) or molecular force sensors.

Interestingly, the elastic modulus of cells correlated with the mechanical properties of the patterned surfaces. Indeed, the P500 pattern has the stiffest pillars (12.3 ± 1.0 N m^{-1}) and, consequently, the highest effective shear modulus (6.9 ± 1.1 MPa). This result appears consistent with previous studies on patterned and non-patterned surfaces that demonstrated that the cell elastic modulus is generally higher and the actin stress fibers are more developed in cells attached to rigid substrates than in cells attached to soft substrates.[72–74]

Interestingly, cells on P1000 often presented a stiffer region in the leading edge of the cell (Figure 7a-6,11,12), which can be ascribed to lamellipodia and could indicate higher persistency and stability of lamellipodia in cells on the P1000 pattern. This observation appears consistent with the increased cell adhesion strength we measured on this pattern. Indeed, lamellipodia high persistency and stability were previously associated with high cell adhesion.[75,76]

3. Summary and Outlook

The behavior of MC3T3-E1 preosteoblast cells during the early interactions with two different arrays of submicron pillars were quantitatively investigated using FluidFM and AFM imaging techniques (**Figure 8**).

The patterns investigated in this study differed with regard with pillar height. The different pillar height resulted in different pillar stiffness, surface shear modulus, and surface roughness. Namely, the pattern with taller pillars had a lower pillar stiffness, a lower surface shear modulus and a higher average surface roughness. These differences induced changes in the cell adhesion strength, cell settling state, cell area, and cell mechanics after 24 h of culture (Figure 8). The cells were smaller and adhered more strongly on the patterns with the taller pillars. This could be explained by the "middle" settling behavior observed for these cells involving attachment of the cell partly on the sidewalls of the pillars, without touching the flat surface between the pillars. This settling behavior resulted in larger normal forces required for the detachment of the cells, as revealed by the FluidFM measurements. The cells on this pattern also revealed a lower elastic modulus above the nucleus associated with less and thinner actin stress fibers visible in this region. However, thicker fibers and a higher elastic modulus were observed at the periphery of the cells, especially at the leading edge of the cell indicating persistence and stability of the lamellipodia that may explain the higher resistance

to shear forces of these cells, as observed during the detachment experiments, and suggesting an enhanced anchorage of the cells on this relatively softer and rougher pattern.

The pattern with the taller pillars showed osteogenic properties in our previous study,[14] as evidenced by the enhanced OPN expression after 21 days of cell culture. The in-depth findings of this study on the effects of pillars height on the early cell interactions indicate that the higher cell adhesion strength induced by the pattern with taller pillars could have favored osteogenic differentiation. This result is consistent with previous observations. Indeed, cells characterized by high adhesion to the substrate (that implies the engagement of integrins and enhanced lamellipodia persistence) and a cytoskeleton under isometric tension were previously associated with high RhoA/ROCK activity,[75,77–80] a major pathway involved in the osteogenic differentiation of MSCs.[81] Furthermore, YAP/TAZ activity was previously shown to be regulated by cell mechanics and to sustain osteogenic differentiation.[82] However, the mechanisms by which RhoA/ROCK and YAP/TAZ activities are regulated by cell adhesion and cell mechanics are still poorly understood. Therefore, further in-depth biochemical analysis focusing on these pathways is fundamental to demonstrate and further understand the relationships between cell adhesion and the osteogenic potential of such topographies.
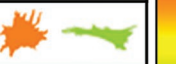
4. Conclusion

In this work, FluidFM and AFM techniques, in combination with optical and SEM, were successfully used to quantify several biophysical characteristics of preosteoblast cells interacting with two different arrays of submicron pillars having the same diameter (200 nm) and interspace (700 nm) but two different pillar heights (500 and 1000 nm).

After 24 h of cell culture, the cells interacting with the pattern with the tallest pillars, that was relatively rougher and softer, exhibited a significantly higher adhesion strength and lower cell area compared to cells cultured on the patterns with shorter pillars. These findings could be explained by the different settling state and cytoskeleton reorganization revealed by the cells cultured on the taller pillars, that influenced the normal forces needed to detach them from the surface and the cellular resistance to shear forces. The implications of the different early cell responses on the osteogenic properties of the patterns are worth for further investigations in the attempt to establish any relationships that could advance the rational design of such surfaces for orthopedic implants.

5. Experimental Section

Fabrication of the Patterns: Arrays of submicron polymeric pillars with a designed diameter of 200 nm, interspace (center-to-center distance) of 700 nm, and two different heights, 500 and 1000 nm, were fabricated by two-photon polymerization (2PP). Following a previously described procedure, the arrays were printed on a glass coverslip using a Photonic Professional GT machine (Nanoscribe, Germany).[14,29] The individual pillars were designed with the help of a computer-aided designed (CAD) software (Solidworks, Dassault Systèmes SE, France). The CAD files were converted to STL files and processed in the DeScribe software

Biophysical parameter	Control	P500	P1000
Cell adhesion strength (24 h)	22 ± 7.5 kPa	21.5 ± 12.5 kPa	32 ± 7 kPa (***)
Cell settling state (24 h)	"bottom"	"bottom"	"middle"
Cell morphology (24 h)			
Cell area (24 h)	3575 ± 2141 μm²	2352 ± 1046 μm² (**)	1390 ± 615 μm² (***)
Cell elastic modulus (above the nucleus) (24 h)	8 ± 3 kPa	19 ± 5 kPa (***)	11 ± 4 kPa
Orientation coherency (above the nucleus) (24 h)	0.55 ± 0.18	0.36 ± 0.16 (**)	0.34 ± 0.22 (***)
Osteogenic differentiation (21 days)	Non-osteogenic[14]	Non-osteogenic[14]	Osteogenic[14]

Figure 8. Summary of the cell biophysical parameters measured after 24 h of cell culture on the osteogenic (P1000) and non-osteogenic (flat control and P500) surfaces. The average value and the standard deviation of the measured parameters are reported. The asterisks indicate the statistical significance of the differences between the various experimental values as compared to the values measured on the flat control surface, retrieved by using the one-way ANOVA test (* $p < 0.1$, ** $p < 0.05$, *** $p < 0.01$). The color of the boxes qualitatively indicates the positive (yellow-red) or negative (light blue and dark blue) variation of the average values of the measured parameters as compared to the average value found on the flat control surface (green), as shown in the scale bar on the right.

(NanoScribe GmbH, Germany). The pillars were printed in Galvo writing mode using the IP-L780 resin (Nanoscribe, Germany), a laser power of 14%, and a writing speed of 1200 μm s⁻¹. The printed area was 500 μm × 500 μm for the samples used for the patterns characterization and 1 mm × 1 mm for the samples used for cell experiments. The samples were developed for 25 min in propylene glycol monomethyl ether acetate (PGMEA, Sigma-Aldrich, Germany), rinsed for 5 min in isopropyl alcohol (IPA, Sigma-Aldrich, Germany), and blow-dried with air. Hereafter, the pattern with a pillar height of 500 nm will be referred to as "P500" and the pattern with a pillar height of 1000 nm as "P1000". For biological experiments, the flat glass coverslip surface was used as a control sample ("C").

Morphological Characterization of the Patterns: 3D topographical images of the patterns were acquired using a JPK Nanowizard 4 AFM (JPK Instruments, Germany) and a high aspect ratio probe (TESPA-HAR, Bruker, Germany). The images were acquired using the Quantitative Imaging (QI) mode and the following parameters: a set point force of 100 nN, a z length of 1500 nm, and a pixel time of 16 ms. The JPK SPM data processing software (JPK instruments, v6.1, Germany) was used to analyze the data. Three 10 μm × 10 μm areas for each sample were analyzed to retrieve the average height of the pillars and the surface roughness (R_a). Three samples for each pattern were analyzed.

A Nova Nano Lab 650 Dual Beam system (FEI, Oregon, USA) was used for SEM analysis of the morphology of the pillars. The specimens were coated with gold (coating thickness ≈ 5 nm) using a sputter coater (JFC-1300, JEOL, Japan) and then imaged by SEM.

Therefore, the top view and 30° tilted images were acquired. The images were analyzed with the ImageJ software (rsb.info.nih.gov/ij/index.html). The base diameters were measured using the top view images. Three samples for each condition and 100 pillars per sample were analyzed.

Mechanical Characterization of the Pillars: The mechanical characterization of single pillars was performed using the previously reported AFM force spectroscopy imaging (FSI) method, which is briefly described in Section S1, Supporting Information.[48] A JPK Nanowizard 4 AFM (JPK Instruments, Germany) was used. The probe was an SSRM-DIA cantilever (Bruker, Billerica, USA) with a cantilever length of 225 μm, a width of 50 μm, a thickness of 5 μm, and a nominal spring constant of 27 N m⁻¹. The probe's tip consisted of a diamond square

pyramid with a height (h_{tip}) of 5.57 μm and a length and width (l_{tip} and $w/2$) of 5 μm.[48,83] The calibration of sensitivity S_z and stiffness constant $k_{c,z}$ of the probe was performed by the thermal tune method.[84]

The analyzed nanopillars were scanned several times in QI mode, with increasing values of the applied force obtained by increasing the set point force until the visible rupture of the nanopillar was observed. The values of maximum lateral force, maximum displacement, adhesion strength, and stiffness of the pillars were calculated as previously reported.[48] The used equations are briefly reported in Section S2, Supporting Information. After each level of applied force, the topography of the same area was acquired in the QI mode, with a low setpoint force (50 nN) to evaluate any possible changes in the morphology of the nanopillars).[48]

The mechanical tests were performed on six pillars of each type (P500 and P1000).

Cell Culture: 5.0×10^4 mouse preosteoblast cells (MC3T3-E1, Sigma-Aldrich, Germany, passage 11) were precultured in a 6-well plate (Greiner Bio-One, Netherlands) in alpha minimum essential medium (α-MEM) (ThermoFisher, US) supplemented with 10% (v/v) fetal bovine serum (FBS, ThermoFisher, US) and 1% (v/v) penicillin-streptomycin (ThermoFisher, US). Cells were incubated at 37 °C, 5% CO_2 (Life Technologies, US) for three to six days. The culture medium was refreshed every 2 days. The specimens were placed into Petri dishes (TPP, Switzerland) and sterilized with 70% ethanol (Sigma-Aldrich, Germany). Cells were detached from the 6-well plate using 100 μL of 0.5% Trypsin-EDTA (TermoFisher Scientific, US) solution (37 °C, 3 min). 7.5×10^4 cells and 5×10^4 cells were seeded on the samples to be analyzed after 4 and 24 h of incubation, respectively.

Immunocytochemistry Analyses: Immunocytochemistry analyses were performed using previously described procedures.[14] The FAs of the cells were stained after 4 and 24 h. Therefore, the specimens were rinsed with PBS, and the cells were fixed using a 4% (v/v) formaldehyde solution (Sigma-Aldrich, Germany). After permeabilization with 0.5% Triton X-100/PBS (Sigma-Aldrich, Germany) at 4 °C for 5 min, the cells were incubated in 1% BSA/PBS (Sigma-Aldrich, Germany) at 37 °C for 5 min. Then, the specimens were incubated in an anti-vinculin mouse monoclonal primary antibody (1:100 in 1% BSA/PBS, Sigma-Aldrich, Germany) for 1 h at 37 °C. The cells were then rinsed thrice with 0.5% Tween-20/PBS (Sigma-Aldrich, Germany) and incubated in Alexa Fluor 488, donkey anti-mouse polyclonal secondary antibody

(1:200 in BSA/PBS, Thermo Fisher, US) for 1 h at room temperature. The specimens were again rinsed thrice with 0.5% Tween-20/PBS for 5 min each time, followed by 5 min rinsing with 1× PBS. Finally, a droplet of 10 µL of ProLong gold (containing 4′,6-diamidino-2-phenylindole, Thermo Fisher, US) was added for nucleus staining. Imaging was performed using a fluorescence microscope (ZOE fluorescent cell imager, Bio-Rad, the Netherlands).

Measurement of Cell Adhesion: A JPK NanoWizard 4 AFM (Bruker-JPK Instruments, Germany), equipped with the CellHesion module and mounted on a Zeiss Axio Observer optical microscope (Carl Zeiss AG, Germany), was used to perform cell adhesion measurements by the FluidFM technique.[39] FluidFM micropipettes (Cytosurge, Switzerland), having a nominal spring constant of 2 N m^{-1}, a length of 200 µm, a width of 36 µm and a microfluidic channel aperture of 8 µm in diameter, were used. The micropipette was connected to an OB1 (Elveflow, France) pressure controller, which was used to apply under- and over-pressure to hold and release the cells.

The probe was calibrated using the thermal method.[84] The JPK petri dish heater maintained the temperature constant during the experiments at 37 °C.

The probe was filled with filtered de-ionized water before the start of experiments to ensure a liquid–liquid interface at the aperture.

The aperture of the micropipette was positioned over the cell nucleus. The cell detachment was performed by setting a force–distance cycle with the following parameters. A set point force of 50 nN and a speed of 1 µm s^{-1} were set to approach the cell. Once the probe was in contact with the cell, a force–constant pause of 10 s was imposed. A negative pressure of −500 mbar or −800 mbar was applied during the pause to grab the cell. At the end of the pause, the probe was retracted at a speed of 1 µm s^{-1}. The z length was set to 80 µm, and the under-pressure was maintained during the retraction.

At the end of the force–distance cycle, a positive pressure of 1 bar was applied to release the cell. However, in most cases, the cells were not wholly detached after applying over-pressure, and an additional cleaning process was required. The cleaning was performed by dipping the probe in 1% Tergazyme (Alconox Inc., USA) solution for 2 min and rinsing it in filtered de-ionized water.

The experiments were performed on 12 cells for each substrate type (the flat glass, used as a control specimen, the P500, and the P1000 patterns) and for two different cell culture times (4 and 24 h). A minimum of 3 or a maximum of 4 samples were analyzed for each tested condition (substrate, culture time). The cells were grown independently on each sample and 4 or 3 cells were analyzed on each sample.

The JPK Data Processing Software was used to analyze the recorded F-d curves and retrieve the adhesion force, that is, the peak force in the retraction segment.

The inverted optical microscope mounted under the AFM in a bright field monitored the cell morphology before and during the experiments. The optical images were analyzed and processed by the ImageJ software (http://rsb.info.nih.gov/ij/index.html).

ImageJ software was used to calculate the total cell surface area and the areas of the elements of the cell surface (circular crowns or elements of circular crowns, with the center corresponding to the center of the aperture and width of 4 µm) used to calculate the adhesion strength as reported in Section S2, Supporting Information.

Characterization of the Cell–Pattern Interface: An SEM (Helios Nano Lab 650, FEI, USA) was used to study the settling state of the cells on the patterned surfaces.

The specimens were rinsed twice with distilled water for 5 min and were dehydrated in 50%, 70% and 96% ethanol solutions for 15, 20 and 20 min, respectively. Finally, the samples were dried overnight at room temperature and were coated with gold (coating thickness ≈ 5 nm) using a sputter coater (JFC-1300, JEOL, Japan).

The experiments were performed on 10 cells for each substrate type (the P500, and the P1000 patterns) after 24 h of cell culture.

Characterization of the Cell Morphology, Cytoskeleton Organization, and Elastic Modulus: Topographical images and mechanical maps of living cells after 4 and 24 h of cell culture were simultaneously acquired using a JPK Nanowizard 4 AFM (Bruker-JPK Instruments, Germany) in the QI mode. A QP-BioAC-CB3 probe (Nanosensors, Switzerland) was used, with a nominal spring constant of 0.06 N m^{-1}, tip radius of 30 nm, cantilever length, and width of 80 and 30 µm, respectively.

The samples were placed in the JPK petri dish heater (JPK Instruments, Germany) to maintain the temperature at 37 °C. The probes' sensitivity and spring constant were calibrated using the thermal noise method.[84] 95 µm × 95 µm areas were scanned with a set point force of 1 nN, corresponding to an indentation depth in the range of 200–1000 nm, a z length value of 2500 nm and a pixel time of 21 ms. The image resolution was set to 256 × 256 pixels.

Data analysis was performed using the JPK postprocessing software (JPK Instruments, Germany) and ImageJ software (http://rsb.info.nih.gov/ij/index.html).

Contact point images that display the height at the zero-force level (i.e., corrected from the indentation depth) were extracted from QI data and used to quantify the maximum and the average height and the area of the analyzed cells. The maximum height was measured at the highest point of the cell, that is, the top of the nucleus. The average height was retrieved as the average value of the heights measured in each pixel of the cell area. The pixels corresponding to the cell area were individuated, defining a threshold value of the height of 50 nm (relative to the substrate). The cell area was calculated as the number of pixels corresponding to the cell times the pixel area.

The experiments were performed on 12 cells for each substrate type (the flat glass, used as a control specimen, the P500, and the P1000 patterns) and for two different cell culture times (4 and 24 h). A minimum of 3 or a maximum of 4 samples were analyzed for each tested condition (substrate, culture time). The cells were grown independently on each sample and 4 or 3 cells for sample were analyzed.

The elastic modulus maps were obtained by fitting the first 200 nm (indentation depth) of the approach segment of the force–distance curves until measured at each point of the scanned area to the Hertz–Sneddon model,[85] considering a paraboloid tip with the nominal tip radius value. The reported values of the elastic modulus were calculated as the average elastic modulus value in the region above the nucleus. The area of interest (above the nucleus) was defined as the area around the highest point of the cell (corresponding to the top of the nucleus), with a height larger than 80% of the maximum height. In this region, the cell height was always larger than 2 µm. Therefore the Hertz condition, namely an indentation depth lower than 10% of the thickness (height) of the sample (cell), was satisfied.

The orientation of the cortex actin fibers in the region above the nucleus was analyzed by processing the mechanical maps using the Dominant Orientation option of the OrientationJ Image J plugin.[86] The retrieved orientation coherency parameter describes the orientation isotropy in the image and ranges from zero (isotropic orientation of structures) to one (highly oriented structures). When parallel actin bundles characterized the analyzed region, the orientation coherency was high. Inversely, the orientation coherency was low when randomly oriented actin fibers populated the studied area.

Statistical Analysis: The significant differences between the means of different experimental groups were individuated by the one-way ANOVA followed by Tukey's multiple pairwise comparisons post hoc test by OriginPro 9.2 software (OriginLab Corporation, Massachusetts, USA).

Supporting Information

Supporting Information is available from the Wiley Online Library or from the author.

Acknowledgements

ADVANCED
SCIENCE NEWS

www.advancedsciencenews.com

NANO · MICRO

small

www.small-journal.com

Conflict of Interest

The authors declare no conflict of interest.

Author Contributions

M.K.G. and L.E.F.-A. contributed equally to this work. L.A., L.E.F.-A., and M.K.G. conceptualized the study. M.N.-G. and B.P. designed and fabricated the patterns under the supervision of L.E.F.-A. and A.A.Z. L.A. and B.P. performed the AFM experiments under the supervision of M.K.G. and L.E.F.-A. M.M. developed cell culture protocols. L.A. post-processed and analyzed the results. L.A. wrote the first draft, which was revised by all the authors.

Data Availability Statement

The data that support the findings of this study are available from the corresponding author upon reasonable request.

Keywords

[1] K. Modaresifar, S. Azizian, M. Ganjian, L. E. Fratila-Apachitei, A. A. Zadpoor, *Acta Biomater.* **2018**, *83*, 29.
[2] M. Mirzaali, I. Van Dongen, N. Tümer, H. Weinans, S. A. Yavari, A. Zadpoor, *Nanotechnology* **2018**, *29*, 43LT02.
[3] K. Modaresifar, L. B. Kunkels, M. Ganjian, N. Tümer, C. W. Hagen, L. G. Otten, P.-L. Hagedoorn, L. Angeloni, M. K. Ghatkesar, L. E. Fratila-Apachitei, A. A. Zadpoor, *Nanomaterials* **2020**, *10*, 347.
[4] A. Rifai, N. Tran, P. Reineck, A. Elbourne, E. Mayes, A. Sarker, C. Dekiwadia, E. P. Ivanova, R. J. Crawford, T. Ohshima, B. C. Gibson, A. D. Greentree, E. Pirogova, K. Fox, *ACS Appl. Mater. Interfaces* **2019**, *11*, 24588.
[5] M. Ganjian, K. Modaresifar, M. R. O. Ligeon, L. B. Kunkels, N. Tümer, L. Angeloni, C. W. Hagen, L. G. Otten, P.-L. Hagedoorn, I. Apachitei, L. E. Fratila-Apachitei, A. A. Zadpoor, *Adv. Mater. Interfaces* **2019**, *6*, 1900640.
[6] K. Modaresifar, M. Ganjian, L. Angeloni, M. Minneboo, M. K. Ghatkesar, P. L. Hagedoorn, L. E. Fratila-Apachitei, A. A. Zadpoor, *Small* **2021**, *17*, 2100706.
[7] F. Y. McWhorter, T. Wang, P. Nguyen, T. Chung, W. F. Liu, *Proc. Natl. Acad. Sci. USA* **2013**, *110*, 17253.
[8] S. N. Christo, A. Bachhuka, K. R. Diener, A. Mierczynska, J. D. Hayball, K. Vasilev, *Adv. Healthcare Mater.* **2016**, *5*, 956.
[9] Y. Hou, W. Xie, L. Yu, L. C. Camacho, C. Nie, M. Zhang, R. Haag, Q. Wei, *Small* **2020**, *16*, 1.
[10] S. G. Higgins, M. Becce, A. Belessiotis-Richards, H. Seong, J. E. Sero, M. M. Stevens, *Adv. Mater.* **2020**, *32*, 1903862.
[11] M. J. Dalby, N. Gadegaard, R. Tare, A. Andar, M. O. Riehle, P. Herzyk, C. D. Wilkinson, R. O. Oreffo, *Nat. Mater.* **2007**, *6*, 997.
[12] S. Dobbenga, L. E. Fratila-Apachitei, A. A. Zadpoor, *Acta Biomater.* **2016**, *46*, 3.
[13] H. Wu, T. Liu, Z. Xu, J. Qian, X. Shen, Y. Li, Y. Pan, D. Wang, K. Zheng, A. R. Boccaccini, J. Wei, *Appl. Mater. Today* **2020**, *18*, 100523.
[14] M. Nouri-Goushki, L. Angeloni, K. Modaresifar, M. Minneboo, P. E. Boukany, M. J. Mirzaali, M. K. Ghatkesar, L. E. Fratila-Apachitei, A. A. Zadpoor, *ACS Appl. Mater. Interfaces* **2021**, *13*, 33767.
[15] A. Trampuz, A. F. Widmer, *Curr. Opin. Infect. Dis.* **2006**, *19*, 349.
[16] U. Filipović, R. G. Dahmane, S. Ghannouchi, A. Zore, K. Bohinc, *Adv. Colloid Interface Sci.* **2020**, *283*, 102228.
[17] M. Ermis, E. Antmen, V. Hasirci, *Bioact Mater* **2018**, *3*, 355.
[18] C. R. Arciola, D. Campoccia, L. Montanaro, *Nat. Rev. Microbiol.* **2018**, 397.
[19] S. Oh, K. S. Brammer, Y. J. Li, D. Teng, A. J. Engler, S. Chien, S. Jin, *Proc. Natl. Acad. Sci. USA* **2009**, *106*, 2130.
[20] M. J. Dalby, N. Gadegaard, R. O. Oreffo, *Nat. Mater.* **2014**, *13*, 558.
[21] T. Sjöström, M. J. Dalby, A. Hart, R. Tare, R. O. Oreffo, B. Su, *Acta Biomater.* **2009**, *5*, 1433.
[22] L. E. McNamara, T. Sjöström, K. E. V. Burgess, J. J. W. Kim, E. Liu, S. Gordonov, P. V. Moghe, R. M. D. Meek, R. O. C. Oreffo, B. Su, M. J. Dalby, *Biomaterials* **2011**, *32*, 7403.
[23] J. Lovmand, J. Justesen, M. Foss, R. H. Lauridsen, M. Lovmand, C. Modin, F. Besenbacher, F. S. Pedersen, M. Duch, *Biomaterials* **2009**, *30*, 2015.
[24] K. W. Kwon, S. S. Choi, B. Kim, S. N. Lee, M. C. Park, P. Kim, S. H. Lee, S. H. Park, K. Y. Suh, *SENSORS, 2006 IEEE*, IEEE, Piscataway, NJ **2006**, pp. 105-108.
[25] P. Zorlutuna, Z. Rong, P. Vadgama, V. Hasirci, *Acta Biomater.* **2009**, *5*, 2451.
[26] J. L. Tan, J. Tien, D. M. Pirone, D. S. Gray, K. Bhadriraju, C. S. Chen, *Proc. Natl. Acad. Sci. USA* **2003**, *100*, 1484.
[27] C. G. Galbraith, M. P. Sheetz, *Proc. Natl. Acad. Sci. USA* **1997**, *94*, 9114.
[28] L. Angeloni, M. Reggente, D. Passeri, M. Natali, M. Rossi, *Wires Nanomed. Nanobiotechnol.* **2018**, *10*, 1.
[29] M. Nouri-Goushki, M. J. Mirzaali, L. Angeloni, D. Fan, M. Minneboo, M. K. Ghatkesar, U. Staufer, L. E. Fratila-Apachitei, A. A. Zadpoor, *ACS Appl. Mater. Interfaces* **2020**, *12*, 200.
[30] M. Reggente, D. Passeri, L. Angeloni, F. A. Scaramuzzo, M. Barteri, F. De Angelis, I. Persiconi, M. E. De Stefano, M. Rossi, *Nanoscale* **2017**, *9*, 5671.
[31] M. Cascione, V. de Matteis, R. Rinaldi, S. Leporatti, *Microsc Res Tech* **2017**, *80*, 109.
[32] A. V. Taubenberger, D. W. Hutmacher, D. J. Muller, *Tissue Eng., Part B* **2014**, *20*, 40.
[33] J. Friedrichs, K. R. Legate, R. Schubert, M. Bharadwaj, C. Werner, D. J. Muller, M. Benoit, *Methods* **2013**, *60*, 169.
[34] K. Haase, A. E. Pelling, *J. R. Soc., Interface* **2015**, *12*, 20140970.
[35] P. Stiefel, F. I. Schmidt, P. Dorig, P. Behr, T. Zambelli, J. A. Vorholt, J. Mercer, *Nano Lett.* **2012**, *12*, 4219.
[36] A. A. Khalili, M. R. Ahmad, *Int. J. Mol. Sci.* **2015**, *16*, 18149.
[37] J. C. Courtenay, J. G. Filgueiras, E. R. deAzevedo, Y. Jin, K. J. Edler, R. I. Sharma, J. L. Scott, *J. Mater. Chem. B* **2019**, *7*, 53.
[38] A. Meister, M. Gabi, P. Behr, P. Studer, J. Voros, P. Niedermann, J. Bitterli, J. Polesel-Maris, M. Liley, H. Heinzelmann, T. Zambelli, *Nano Lett.* **2009**, *9*, 2501.
[39] E. Potthoff, O. Guillaume-Gentil, D. Ossola, J. Polesel-Maris, S. LeibundGut-Landmann, T. Zambelli, J. A. Vorholt, *PLoS One* **2012**, *7*, e52712.
[40] E. Potthoff, D. Ossola, T. Zambelli, J. A. Vorholt, *Nanoscale* **2015**, *7*, 4070.

[41] O. Guillaume-Gentil, E. Potthoff, D. Ossola, C. M. Franz, T. Zambelli, J. A. Vorholt, *Trends Biotechnol.* **2014**, *32*, 381.

[42] S. Sankaran, L. Jaatinen, J. Brinkmann, T. Zambelli, J. Voros, P. Jonkheijm, *ACS Nano* **2017**, *11*, 3867.

[43] N. Cohen, S. Sarkar, E. Hondroulis, P. Sabhachandani, T. Konry, *Talanta* **2017**, *174*, 409.

[44] J. Dehullu, J. A. Vorholt, P. N. Lipke, Y. F. Dufrene, *Trends Microbiol.* **2019**, *27*, 728.

[45] P. Wysotzki, A. Sancho, J. Gimsa, J. Groll, *Colloids Surf., B* **2020**, *190*, 110894.

[46] L. Hofherr, C. Muller-Renno, C. Ziegler, *PLoS One* **2020**, *15*, e0227395.

[47] X. Q. Zhou, Y. H. Hou, J. Q. Lin, *AIP Adv.* **2015**, *5*, 1.

[48] L. Angeloni, M. Ganjian, M. Nouri-Goushki, M. J. Mirzaali, C. W. Hagen, A. A. Zadpoor, L. E. Fratila-Apachitei, M. K. Ghatkesar, *Addit. Manuf.* **2021**, 39.

[49] F. C. Chien, C. W. Kuo, Z. H. Yang, D. Y. Chueh, P. Chen, *Small* **2011**, *7*, 2906.

[50] S. Hong, E. Ergezen, R. Lec, K. A. Barbee, *Biomaterials* **2006**, *27*, 5813.

[51] A. Taubenberger, D. A. Cisneros, J. Friedrichs, P. H. Puech, D. J. Muller, C. M. Franz, *Mol. Biol. Cell* **2007**, *18*, 1634.

[52] W. Huang, B. Anvari, J. H. Torres, R. G. LeBaron, K. A. Athanasiou, *J. Orthop. Res.* **2003**, *21*, 88.

[53] R. G. LeBaron, K. A. Athanasiou, *Biomaterials* **2000**, *21*, 2575.

[54] E. Potthoff, D. Franco, V. D'Alessandro, C. Starck, V. Falk, T. Zambelli, J. A. Vorholt, D. Poulikakos, A. Ferrari, *Nano Lett.* **2014**, *14*, 1069.

[55] C. Wu, M. Chen, T. Zheng, X. Yang, *Biomed. Mater. Eng.* **2015**, *26*, S155.

[56] A. V. Taubenberger, M. A. Woodruff, H. Bai, D. J. Muller, D. W. Hutmacher, *Biomaterials* **2010**, *31*, 2827.

[57] J. Markwardt, J. Friedrichs, C. Werner, A. Davids, H. Weise, R. Lesche, A. Weber, U. Range, H. Meißner, G. Lauer, B. Reitemeier, *J. Biomed. Mater. Res., Part A* **2014**, *102*, 1422.

[58] J. Zhou, X. Zhang, J. Sun, Z. Dang, J. Li, X. Li, T. Chen, *Phys. Chem. Chem. Phys.* **2018**, *20*, 22946.

[59] N. Buch-Månson, S. Bonde, J. Bolinsson, T. Berthing, J. Nygård, K. L. Martinez, *Adv. Funct. Mater.* **2015**, *25*, 3246.

[60] L. Dao, C. Gonnermann, C. M. Franz, *J. Mol. Recognit.* **2013**, *26*, 578.

[61] W. K. Szeto, M. Y. Xie, J. K. Kim, M. M. F. Yuen, P. Tong, S. Yi, *Int. Symp. Electron. Mater. Packag. (EMAP2000)*, **2000**, pp. 263–268.

[62] A. Mogilner, K. Keren, *Curr. Biol.* **2009**, *19*, R762.

[63] S. Romero, C. Le Clainche, A. M. Gautreau, *Biochem. J.* **2020**, *477*, 1.

[64] T. Iba, B. E. Sumpio, *Microvasc. Res.* **1991**, *42*, 245.

[65] C. R. Guerrero, P. D. Garcia, R. Garcia, *ACS Nano* **2019**, *13*, 9629.

[66] M. Fritzsche, D. Li, H. Colin-York, V. T. Chang, E. Moeendarbary, J. H. Felce, E. Sezgin, G. Charras, E. Betzig, C. Eggeling, *Nat. Commun.* **2017**, *8*, 14347.

[67] L. Haviv, Y. Brill-Karniely, R. Mahaffy, F. Backouche, A. Ben-Shaul, T. D. Pollard, A. Bernheim-Groswasser, *Proc. Natl. Acad. Sci. USA* **2006**, *103*, 4906.

[68] Y. Ideses, Y. Brill-Karniely, L. Haviv, A. Ben-Shaul, A. Bernheim-Groswasser, *PLoS One* **2008**, *3*, e3297.

[69] M. Soares e Silva, M. Depken, B. Stuhrmann, M. Korsten, F. C. MacKintosh, G. H. Koenderink, *Proc. Natl. Acad. Sci. USA* **2011**, *108*, 9408.

[70] S. L. Lee, A. Nekouzadeh, B. Butler, K. M. Pryse, W. B. McConnaughey, A. C. Nathan, W. R. Legant, P. M. Schaefer, R. B. Pless, E. L. Elson, G. M. Genin, *PLoS One* **2012**, *7*, e45512.

[71] C. Y. Lee, J. Lou, K. K. Wen, M. McKane, S. G. Eskin, S. Ono, S. Chien, P. A. Rubenstein, C. Zhu, L. V. McIntire, *Proc. Natl. Acad. Sci. USA* **2013**, *110*, 5022.

[72] B. Geiger, J. P. Spatz, A. D. Bershadsky, *Nat. Rev. Mol. Cell Biol.* **2009**, *10*, 21.

[73] D. E. Discher, P. Janmey, Y. L. Wang, *Science* **2005**, *310*, 1139.

[74] T. Yeung, P. C. Georges, L. A. Flanagan, B. Marg, M. Ortiz, M. Funaki, N. Zahir, W. Ming, V. Weaver, P. A. Janmey, *Cell Motil. Cytoskeleton* **2005**, *60*, 24.

[75] B. Borm, R. P. Requardt, V. Herzog, G. Kirfel, *Exp. Cell Res.* **2005**, *302*, 83.

[76] G. Giannone, B. J. Dubin-Thaler, O. Rossier, Y. Cai, O. Chaga, G. Jiang, W. Beaver, H. G. Dobereiner, Y. Freund, G. Borisy, M. P. Sheetz, *Cell* **2007**, *128*, 561.

[77] E. J. Arnsdorf, P. Tummala, R. Y. Kwon, C. R. Jacobs, *J. Cell Sci.* **2009**, *122*, 546.

[78] E. C. Lessey, C. Guilluy, K. Burridge, *Biochemistry* **2012**, *51*, 7420.

[79] X. D. Ren, W. B. Kiosses, M. A. Schwartz, *EMBO J.* **1999**, *18*, 578.

[80] K. Bhadriraju, M. Yang, S. Alom Ruiz, D. Pirone, J. Tan, C. S. Chen, *Exp. Cell Res.* **2007**, *313*, 3616.

[81] R. McBeath, D. M. Pirone, C. M. Nelson, K. Bhadriraju, C. S. Chen, *Dev. Cell* **2004**, *6*, 483.

[82] A. Totaro, T. Panciera, S. Piccolo, *Nat. Cell Biol.* **2018**, *20*, 888.

[83] M. Ganjian, L. Angeloni, M. J. Mirzaali, K. Modaresifar, C. W. Hagen, M. K. Ghatkesar, P. L. Hagedoorn, L. E. Fratila-Apachitei, A. A. Zadpoor, *Nanoscale* **2020**, *12*, 21988.

[84] S. Belikov, J. Alexander, C. Wall, I. Yermolenko, S. Magonov, I. Malovichko, *2014 Am. Control Conf*, **2014**, pp. 1009-1014.

[85] I. N. Sneddon, *Int. J. Eng. Sci.* **1965**, *3*, 47.

[86] F. Eghiaian, A. Rigato, S. Scheuring, *Biophys. J.* **2015**, *108*, 1330.